A generalized Peierls-Nabarro model for curved dislocations and core structures of dislocation loops in Al and Cu

Yang Xiang [1,*], He Wei [2], Pingbing Ming [3], Weinan E [4]

Abstract

In this paper, we present a generalized Peierls-Nabarro model for curved dislocations. In the generalized Peierls-Nabarro model, the anisotropic elastic energy is obtained efficiently by solving the elasticity system associated with the disregistry across the slip plane using the Fast Fourier Transform (FFT) method, and the generalized stacking fault energy is used for the interplanar potential across the slip plane. Simulation results are reported on the core structures and the activation energies of dislocation loops in Al and Cu, incorporating both the elastic anisotropy and the full disregistry vector in the slip plane.

Key words: Dislocation; dislocation structures; micromechanical modeling; Peierls-Nabarro model

* Corresponding author. Email address: maxiang@ust.hk
[1] Department of Mathematics, The Hong Kong University of Science and Technology, Clear Water Bay, Kowloon, Hong Kong
[2] School of Mathematical Sciences, Peking University, Beijing 100871, China
[3] Institute of Computational Mathematics and Scientific/Engineering Computing, Academy of Mathematics and System Sciences, Chinese Academy of Sciences, No.55 Zhong-Guan-Cun East Road, Beijing 100080, China
[4] Department of Mathematics and PACM, Princeton University, Princeton, NJ 08544, U.S.A.

1 Introduction

To model dislocations, the long-ranged elastic field of a dislocation is very well described by the continuum elasticity theory outside a small region surrounding the dislocation, which is the core region of the dislocation; inside the core region, the heavily distorted atomic structure requires atomistic models, and strongly influences the dislocation mobility and the mechanical behavior of the materials [1]. The Peierls-Nabarro model [1–3] is a hybrid model that incorporates the atomic features into the continuum framework.

In the framework of the Peierls-Nabarro model, the solid is divided by the slip plane of the dislocation into two half-space linear elastic continua, which have a disregistry (misfit) relative to each other and are connected by a nonlinear potential force. In the classical Peierls-Nabarro model [1–3], isotropic linear elasticity is used in the two half-space elastic continua, and the interplanar potential is approximated by the simple Frenkel sinusoidal function [4]. The analytical solution of the classical Peierls-Nabarro model gives qualitative descriptions for the dislocation core profile as well as the energy barrier (Peierls energy) and the critical stress (Peierls stress) for the motion of dislocations.

The Peierls-Nabarro model has been improved greatly in the subsequent work, especially with the introduction of the generalized stacking fault energy for the atomic interaction across the slip plane [5] and the availability of the accurate results based on *ab initio* calculations [6–11]. It has been argued in these references that using the generalized stacking fault energy obtained from *ab inito* calculations, the Peierls-Nabarro model can give more reliable results than the atomistic simulations using empirical potentials. Using the generalized stacking fault energy, no analytical solution of the Peierls-Nabarro model is available, and several numerical solution methods were proposed to obtain the dislocation profile, such as the arctangent type basis functions [7,12,13] and the semidiscrete Peierls-Nabarro model [9]. Another improvement of the Peierls-Nabarro model is to include the full elastic anisotropy [12,14,15], which is important for materials with strong anisotropic effect (e.g. Cu) [1]. Other efforts to improve the Peierls-Nabarro model can be found on incorporating the discreteness of the crystal lattices [9,16,17], the nonlocal effect near the slip plane [18], and the disregistry normal to the slip plane (opening) [9]. The major limitation of the Peierls-Nabarro model lies in the underlying assumption that the nonlinear interaction is restricted to the slip plane, which makes this model work well only for dislocations with planar cores such as those in FCC materials. Several attempts

have been made to generalize the Peierls-Nabarro model to the nonplanar core of screw dislocations in BCC materials [19] and cross-slip of screw dislocations to different slip planes in FCC materials [20].

All these Peierls-Nabarro models mentioned above are for straight dislocations. In reality, dislocations are curved and commonly form loops inside crystalline materials. Only a few attempts have been made to study the core structure and detailed dynamics of curved dislocations within the framework of the Peierls-Nabarro models. In [21], a variational boundary integral method [22,23] was used to study the homogeneous nucleation of dislocation loops under stress. In this model, the elastic energy was obtained by treating the displacement discontinuity on the slip plane as a continuous distribution of dislocation loops [1,24]; the interplanar misfit energy was obtained using Rice's modification of the Frenkel relation for dislocations nucleated from the crack tips [25]; and the resulting singular integral equation was solved by a finite element based method [22]. In [26], two-dimensional lattice models were introduced to study the motion of a dislocation kink. In [27], a hybrid model incorporating the Peierls-Nabarro framework into a dislocation dynamics model was proposed, in which N dislocation loops (about 20 in their examples) were used to represent the core structure of one single loop. The elastic energy of a dislocation loop was calculated by summing the interaction between each segment pairs on all N loops; and the restoring force due to the generalized stacking fault energy obtained from *ab initio* calculations [11] was calculated by representing disregistry across the slip plane using step function approximation. However, although elastic anisotropy was included in the formulation in some of these models, their simulations were all performed in isotropic media. Besides, in the simulations in [21,27], the disregistry across the slip plane was restricted in the direction of the Burgers vector (the constrained path approximation [25]), thus the dissociation of dislocations into partials was not included.

In this paper, we use a generalized Peierls-Nabarro model to study the core structures and properties of dislocation loops in Al and Cu, incorporating both the elastic anisotropy and the full disregistry vector in the slip plane, which to our knowledge has never been done in simulations within the framework of Peierls-Nabarro model in the literature. In the generalized Peierls-Nabarro model, the distribution of the dislocations is represented by the disregistry across the slip plane that is allowed to be in any direction [21–23,26,29,33]. The anisotropic elastic energy is obtained by solving the elasticity system associated with the disregistry using the Fast Fourier Transform (FFT) method. The generalized stacking

fault energy is used for the interplanar potential across the slip plane. The resulting nonlinear equations for the distribution of the dislocations are solved by minimizing the total energy.

Compared with the finite element formulation in [21], besides the usual advantages of efficiency and simplicity in formulation and programming that the FFT methods have over the finite element methods, our FFT based method also avoids the singularities in calculating the stress field associated with dislocations that all formulations in physical space have [1,24] including the finite element formulation in [21]. The efficiency for a two dimensional Peierls-Nabarro model is crucial, especially when computing the core structure of dislocation loops in a crystal such as Cu, in which the two partials in a dislocation loop have large separation thus large simulation cells are required. Compared with the interaction summation over small segments on dislocation loop arrays in the hybrid model in [27], our FFT method is simpler and describes the dislocation structure more accurately. Besides, the hybrid model in [27] works only under the constrained path approximation for curved dislocations.

Note that the purpose of our method is different from that of the phase field models in [28,29], which aimed at the dynamics of dislocation ensembles, and in which the interplanar potentials were used only for regularization. The three dimensional phase field model in [28] has also been generalized to study the dislocation dissociation in FCC crystals incorporating the generalized stacking fault energy [30]. However, when applied to the dislocation core structures in a particular slip plane, it is not as accurate as the classical Peierls-Nabarro model. In particular, their model contains a gradient energy term that is not included in the classical Peierls-Nabarro model, and which has been shown to change the dislocation core profile [30]. Besides, they do not directly use the disregistry across the slip plane to represent dislocations, and it is not easy to incorporate the opening in their model.

2 The generalized Peierls-Nabarro model

In this section, we present the formulation for the generalized Peierls-Nabarro model. Suppose that the slip plane of the dislocation is located at $z = 0$, and the disregistry of the upper half crystal relative to the lower half is $(\phi(x, y), \psi(x, y), 0)$. The total energy in

the framework of the Peierls-Nabarro models [1–3] can be written as

$$E = E_{\text{elastic}} + E_{\text{misfit}}. \tag{1}$$

The energy E_{elastic} is the elastic energy in the two half-space linear elastic continua,

$$E_{\text{elastic}} = \int_{\mathbf{R}^3} \sum_{i,j=1}^{3} \frac{1}{2} \sigma_{ij} \epsilon_{ij} dx dy dz, \tag{2}$$

where $\{\sigma_{ij}\}$ and $\{\epsilon_{ij}\}$ are the stress and strain tensors, respectively, and $\sigma_{ij} = \sum_{k,l=1}^{3} C_{ijkl} \epsilon_{kl}$, for $i, j = 1, 2, 3$, where $\{C_{ijkl}\}$ is the elastic constant tensor. Using the dislocation density tensor $\{a_{ij}\}$ [31–33], which in this problem is

$$\{a_{ij}\} = \begin{pmatrix} \phi_y(x,y)\delta(z) & \psi_y(x,y)\delta(z) & 0 \\ -\phi_x(x,y)\delta(z) & -\psi_x(x,y)\delta(z) & 0 \\ 0 & 0 & 0 \end{pmatrix}, \tag{3}$$

the stress can be expressed using Mura's formula in Fourier space [33]:

$$\widehat{\sigma}_{mn}(k_1, k_2, k_3) = \sum_{j,l,p,q,r,s,t=1}^{3} \epsilon_{jst} C_{mnjl} C_{pqrs} i k_q \frac{N_{lp}(k_1, k_2, k_3)}{D(k_1, k_2, k_3)} \widehat{a}_{tr}(k_1, k_2, k_3), \tag{4}$$

where (k_1, k_2, k_3) are the frequencies in Fourier space, $\widehat{\sigma}_{ij}$ and $\widehat{a}_{ij}$ are the Fourier transform of σ_{ij} and a_{ij}, respectively, $D(k_1, k_2, k_3)$ is the determinant of the matrix $\left\{ \sum_{m,n=1}^{3} C_{imjn} k_m k_n \right\}$ and $\{N_{ij}(k_1, k_2, k_3)\}$ is its adjoint matrix. The nonsingularity of the stress field in the above formulation is guaranteed by the fact that the matrix $\left\{ \sum_{m,n=1}^{3} C_{imjn} k_m k_n \right\}$ is positive definite [39]. The average of the stress in a simulation cell is determined by the applied field.

The energy E_{misfit} is the misfit energy due to the nonlinear atomic interaction across the slip plane

$$E_{\text{misfit}} = \int_{\mathbf{R}^2} \gamma(\phi(x,y), \psi(x,y)) dx dy, \tag{5}$$

where $\gamma(\phi, \psi)$ is the generalized stacking fault energy [5], which can be obtained accurately

using interatomic potentials or *ab initio* calculations [5–11]. The generalized stacking fault energy can be expressed using truncated Fourier series [8,12,13,34] or symmetrized polynomial basis [11] based on the crystal lattice symmetry, or by tabulated values. Any of these forms can be used in our model.

The minimum energy state with respect to ϕ and ψ gives the equilibrium distribution of the Burgers vector of the dislocations, which can be shown to satisfy the following Euler-Lagrange equations

$$\frac{\delta E}{\delta \phi} = \sigma_{13} + \frac{\partial \gamma}{\partial \phi} = 0, \quad \frac{\delta E}{\delta \psi} = \sigma_{23} + \frac{\partial \gamma}{\partial \psi} = 0, \tag{6}$$

where σ_{13} and σ_{23} are the stress on the $z = 0$ plane. Note that the stress in these equilibrium equations includes both the stress generated by the dislocations and the applied stress.

For the stress components in Eq. (6), using Eqs. (3) and (4), we can write

$$\widehat{\sigma}_{mn}(k_1, k_2) = \widehat{F}_{mn}(k_1, k_2)\widehat{\phi}(k_1, k_2) + \widehat{G}_{mn}(k_1, k_2)\widehat{\psi}(k_1, k_2), \tag{7}$$

where

$$\widehat{F}_{mn}(k_1, k_2) = \int_{\mathbf{R}} \sum_{j,l,p,q,s=1}^{3} C_{mnjl} C_{pq1s} k_q \frac{N_{lp}(k_1, k_2, k_3)}{2\pi D(k_1, k_2, k_3)} (\epsilon_{js2} k_1 - \epsilon_{js1} k_2) dk_3, \tag{8}$$

$$\widehat{G}_{mn}(k_1, k_2) = \int_{\mathbf{R}} \sum_{j,l,p,q,s=1}^{3} C_{mnjl} C_{pq2s} k_q \frac{N_{lp}(k_1, k_2, k_3)}{2\pi D(k_1, k_2, k_3)} (\epsilon_{js2} k_1 - \epsilon_{js1} k_2) dk_3. \tag{9}$$

Note that even though Eq. (7) is derived from three dimensional formulation for elasticity, the expression itself is defined only on the slip plane of the dislocation. For simplicity of notations, we write $\sigma_{mn}(x, y, 0)$ as $\sigma_{mn}(x, y)$, and the Fourier transform in Eqs. (7)–(9) is in two dimensions. It is easy to verify that for straight dislocations with isotropic elasticity, this formulation reduces to that of the classical Peierls-Nabarro model [1–3]. Equivalent formulations or formulations for isotropic elasticity have been obtained and used in [21–23,26,29].

In some crystals such as Si, the disregistry normal to the slip plane (the opening) is also very important [8,9]. This effect can be included in the elasticity system by considering full disregistry $(\phi(x, y), \psi(x, y), \eta(x, y))$, where $\eta(x, y)$ is the opening across the slip plane.

In this case, the dislocation density tensor becomes

$$\{a_{ij}\} = \begin{pmatrix} \phi_y(x,y)\delta(z) & \psi_y(x,y)\delta(z) & \eta_y(x,y)\delta(z) \\ -\phi_x(x,y)\delta(z) & -\psi_x(x,y)\delta(z) & -\eta_x(x,y)\delta(z) \\ 0 & 0 & 0 \end{pmatrix}. \tag{10}$$

The generalized stacking fault energy with the effect of opening $\gamma(\phi,\psi,\eta)$ can be obtained from interatomic potentials or *ab initio* calculations [9], or using the universal binding energy curves [35–38]. The minimum energy state in this case satisfies

$$\frac{\partial E}{\partial \phi} = \sigma_{13} + \frac{\partial \gamma}{\partial \phi} = 0, \quad \frac{\partial E}{\partial \psi} = \sigma_{23} + \frac{\partial \gamma}{\partial \psi} = 0, \quad \frac{\partial E}{\partial \eta} = \sigma_{33} + \frac{\partial \gamma}{\partial \eta} = 0, \tag{11}$$

in which the stress components can be calculated using the following equations:

$$\widehat{\sigma}_{mn}(k_1,k_2) = \widehat{F}_{mn}(k_1,k_2)\widehat{\phi}(k_1,k_2) + \widehat{G}_{mn}(k_1,k_2)\widehat{\psi}(k_1,k_2) + \widehat{H}_{mn}(k_1,k_2)\widehat{\eta}(k_1,k_2), \tag{12}$$

where in the new term containing $\widehat{\eta}(k_1,k_2)$,

$$\widehat{H}_{mn}(k_1,k_2) = \int_{\mathbf{R}} \sum_{j,l,p,q,s=1}^{3} C_{mnjl} C_{pq3s} k_q \frac{N_{lp}(k_1,k_2,k_3)}{2\pi D(k_1,k_2,k_3)} (\epsilon_{js2}k_1 - \epsilon_{js1}k_2) dk_3. \tag{13}$$

Numerically, the solution of Eq. (6) (or Eq. (11)) is found by minimizing the total energy in Fourier space under periodic boundary conditions in the steepest descent direction, i.e., solving the equations $\frac{\partial \phi}{\partial t} = -\frac{\partial E}{\partial \phi}$, $\frac{\partial \psi}{\partial t} = -\frac{\partial E}{\partial \psi}$ (and $\frac{\partial \eta}{\partial t} = -\frac{\partial E}{\partial \eta}$) in Fourier space to the equilibrium state, where t is an artificial time. The stress components in Eq. (6) (or Eq. (11)) are calculated using the FFT method through Eqs. (7)–(9) (or Eqs. (8),(9),(12), and (13)). The integrals with respect to k_3 in $\widehat{F}_{mn}(x,y)$, $\widehat{G}_{mn}(x,y)$ (and $\widehat{H}_{mn}(x,y)$) are replaced by summations over integer values of k_3. These summations are the same for the same type of slip planes in a crystal, e.g., $\{111\}$ slip planes in an FCC crystal, thus they can be pre-calculated only once before the energy minimization. Smooth profiles of the disregistry components that are close to the solutions for the perfect or partial dislocations, such as the arctangent profiles in the classical Peierls-Nabarro model [1–3], can be used as the initial conditions for the energy minimization.

It is a standard technique to make the effect of periodic images negligible by using a

large simulation cell, for which further increasing the size only gives negligible changes in the result. Especially, since the summation with respect to k_3 is performed only once before the energy minimization, the size of the simulation cell in the z direction can be chosen much larger to make the periodic effect in the z direction arbitrarily small. The choice of the length of Burgers vector is a compromise between the resolution of the dislocation core, which requires more numerical grid points for the length of the Burgers vector, and the size of the simulation cell, which requires that the length of the Burgers vector relative to the cell size cannot be quite large to eliminate the effect of the periodic boundary conditions. In practice, the Burgers vector can be chosen to be several numerical grid constants.

3 Formulation and parameters for FCC Al and Cu

In this paper, we use our method to study the core structures of dislocation loops on the (111) planes of FCC Al and Cu. The effect of opening is neglected. The dislocations have Burgers vector $\mathbf{b} = \frac{a}{2}[\bar{1}10]$. A perfect dislocation with this Burgers vector in most FCC crystals tends to dissociate into Shockley partials [1]: $\frac{a}{2}[\bar{1}10] \longrightarrow \frac{a}{6}[\bar{1}2\bar{1}] + \frac{a}{6}[\bar{2}11]$.

We use the following parameters. The lattice constant a is $0.405nm$ for Al and $0.361nm$ for Cu. The elastic constants $C_{11} = 10.82 \times 10^{10}Pa$, $C_{12} = 6.13 \times 10^{10}Pa$, and $C_{44} = 2.85 \times 10^{10}Pa$ for Al, and $C_{11} = 16.84 \times 10^{10}Pa$, $C_{12} = 12.14 \times 10^{10}Pa$, $C_{44} = 7.54 \times 10^{10}Pa$ for Cu [1].

We use the following truncated Fourier expansion for the generalized stacking fault energy

$\gamma(\phi,\psi)$ on FCC (111) planes, which incorporates the symmetry of the crystal lattice [34]:

$$\begin{aligned}\gamma(\phi,\psi) = \quad & c_0 \\ & +c_1\Big(\cos\tfrac{2\pi}{b}(\phi+\psi/\sqrt{3})+\cos\tfrac{2\pi}{b}(\phi-\psi/\sqrt{3})+\cos\tfrac{4\pi\psi}{\sqrt{3}b}\Big) \\ & +c_2\Big(\cos\tfrac{2\pi}{b}(\phi+\sqrt{3}\psi)+\cos\tfrac{2\pi}{b}(\phi-\sqrt{3}\psi)+\cos\tfrac{4\pi\phi}{b}\Big) \\ & +c_3\Big(\cos\tfrac{2\pi}{b}(2\phi+2\psi/\sqrt{3})+\cos\tfrac{2\pi}{b}(2\phi-2\psi/\sqrt{3})+\cos\tfrac{8\pi\psi}{\sqrt{3}b}\Big) \\ & +d_1\Big(\sin\tfrac{2\pi}{b}(\phi-\psi/\sqrt{3})-\sin\tfrac{2\pi}{b}(\phi+\psi/\sqrt{3})+\sin\tfrac{4\pi\psi}{\sqrt{3}b}\Big) \\ & +d_2\Big(\sin\tfrac{2\pi}{b}(2\phi-2\psi/\sqrt{3})-\sin\tfrac{2\pi}{b}(2\phi+2\psi/\sqrt{3})+\sin\tfrac{8\pi\psi}{\sqrt{3}b}\Big),\end{aligned} \tag{14}$$

where ϕ is the disregistry in the $[\bar{1}10]$ direction, ψ is the disregistry in the $[\bar{1}\bar{1}2]$ direction, b is the length of the Burgers vector, and $c_0 = -3c_1 - 3c_2 - 3c_3$. For Al, the coefficients $c_1 = -0.0595J/m^2$, $c_2 = -0.003J/m^2$, $c_3 = -0.0109J/m^2$, $d_1 = -0.0426J/m^2$, $d_2 = 0.0153J/m^2$; and for Cu, $c_1 = -0.0876J/m^2$, $c_2 = 0$, $c_3 = -0.0186J/m^2$, $d_1 = -0.1517J/m^2$, $d_2 = 0.0149J/m^2$. These values of the coefficients are obtained by fitting available data for the elastic constants in the (111) plane, the stacking fault energy, the unstable stacking fault energy in the $< 112 >$ direction, and the unstable stacking fault energy in the $< 110 >$ direction (only for Al) [1,11,40], following [12]. The obtained $\gamma(\phi,\psi)$ for Al and Cu are shown in Fig. 1.

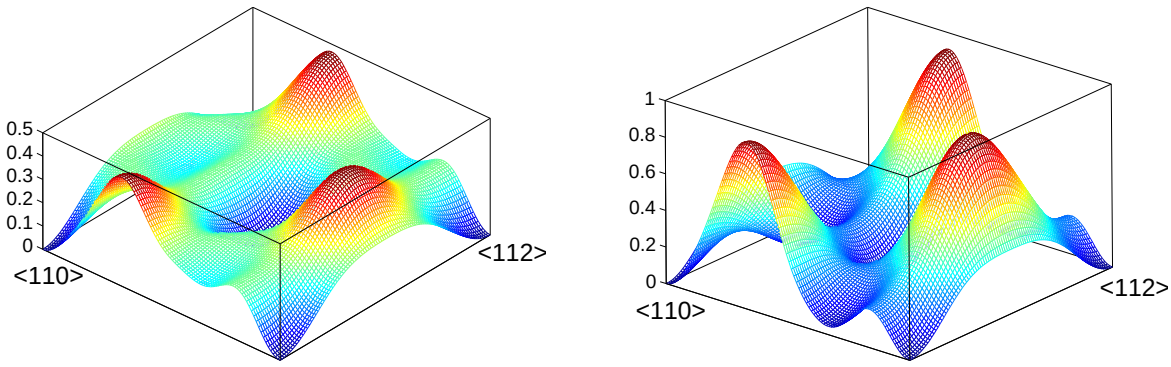

(a) $\gamma(\phi,\psi)$ on Al (111) plane (b) $\gamma(\phi,\psi)$ on Cu (111) plane

Fig. 1. The generalized stacking fault energy $\gamma(\phi,\psi)$ (Unit: J/m^2).

In the simulation results reported in this paper, the size of the simulation cell is 1024×1024 grid points, and the length of the Burgers vector $b = 4\Delta x$ ($b = 2\Delta x$ for very large

dislocation loops in Cu), where $\Delta x = \Delta y$ is the grid size. We use 16384 grid points in the summation in the z direction. Further modifications of these parameters to increase the accuracy only give negligible changes in the results.

4 Straight dislocations

When applied to straight dislocations, our FFT method, in which only one dimensional FFT needs to be performed, is an alternative to the currently available numerical methods within the framework of the Peierls-Nabarro model [7,9,11,12], In this section, we present the simulation results of the core structures of straight dislocations in Al and Cu using our method, and compare them with the results obtained using other Peierls-Nabarro models and those from experiments.

We choose the direction of the straight dislocations to be the y axis. If θ is the angle between the dislocation line and the Burgers vector, we have $\phi = \phi_1 \sin\theta + \psi_1 \cos\theta$ and $\psi = -\phi_1 \cos\theta + \psi_1 \sin\theta$, where (ϕ, ψ) and (ϕ_1, ψ_1) are the coordinates of the disregistry vector in the coordinate systems described in the previous and this sections, respectively. To enforce periodic boundary conditions for straight dislocations, a pair of dislocations with opposite directions are placed in one periodic cell by a distance equal to half of the cell size. Convergence tests show that the effect on the core structure of one dislocation from the other and all the periodic images is negligible for the cells we have chosen for the simulations (see previous section). The density of dislocation, or the distribution of the Burgers vector, is the derivative of the disregistry in the direction perpendicular to the dislocation [1]: $\rho(x) = \phi'(x) = \phi_1'(x)\sin\theta + \psi_1'(x)\cos\theta$, where the derivatives can be calculated using FFT. Even though one dimensional model is enough for these straight dislocations, we solved these examples in two dimensions as test examples for the full two dimensional model.

We first present a numerical test for a straight screw dislocation in an FCC crystal using anisotropic elasticity and the Frenkel sinusoidal potential $\gamma(\psi_1) = \frac{C'_{44}b^2}{4\pi^2 d}(1 - \cos\frac{2\pi\psi_1}{b})$, when the classical Peierls-Nabarro model has an analytical solution for the dislocation density [1]: $\rho(x) = \frac{b}{\pi}\frac{\xi}{x^2+\xi^2}$, where $\xi = \frac{d}{2C'_{44}}\sqrt{C'_{44}\frac{C'_{11}-C'_{12}}{2} - C'^2_{14}}$, C'_{11}, C'_{12}, C'_{14}, and C'_{44} are the elastic constants of the FCC crystal in the coordinate system described above, and d is the interplanar distance in the [111] direction. Figure 2 shows the calculated dislocation

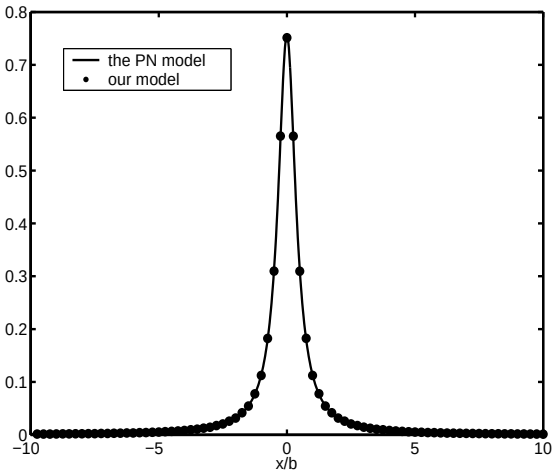

Fig. 2. Under the conditions of anisotropic elasticity and Frenkel sinusoidal potential, the dislocation density of a screw dislocation obtained using our model (dots) and the result of the classical Peierls-Nabarro (PN) model (solid line), using parameters of Cu.

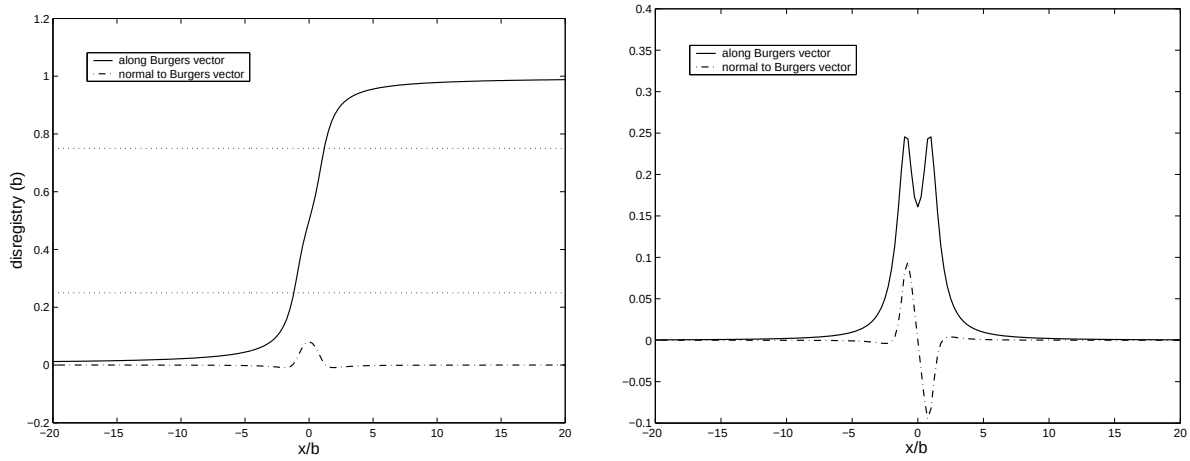

(a) Disregistry (b) Dislocation density

Fig. 3. The core structure of a straight edge dislocation in Al. Solid line: the component parallel to the Burgers vector; Dash-dot line: the component perpendicular to the Burgers vector. The dotted lines in (a) show the values $\frac{1}{4}b$ and $\frac{3}{4}b$.

density using our model under these conditions and the dislocation density given by the above analytical expression, using parameters of Cu. The excellent agreement shows that our model calculate the solutions accurately for straight dislocations in anisotropic media, and recovers the available results of the classical Peierls-Nabarro model if the same conditions are used.

The core structure of a straight edge dislocation in Al obtained using our model is shown in Fig. 3. The two Shockley partials in these dislocations overlap heavily, and only the tendency for dissociation is observed. The results of the core width of different kinds of

Table 1
The core width/partial separation of straight dislocations in Al and Cu (in nm).

	edge	60^o	30^o	screw
Core width in Al	0.68	0.60	0.48	0.42
Partial separation in Cu	3.6	3.1	1.8	1.1

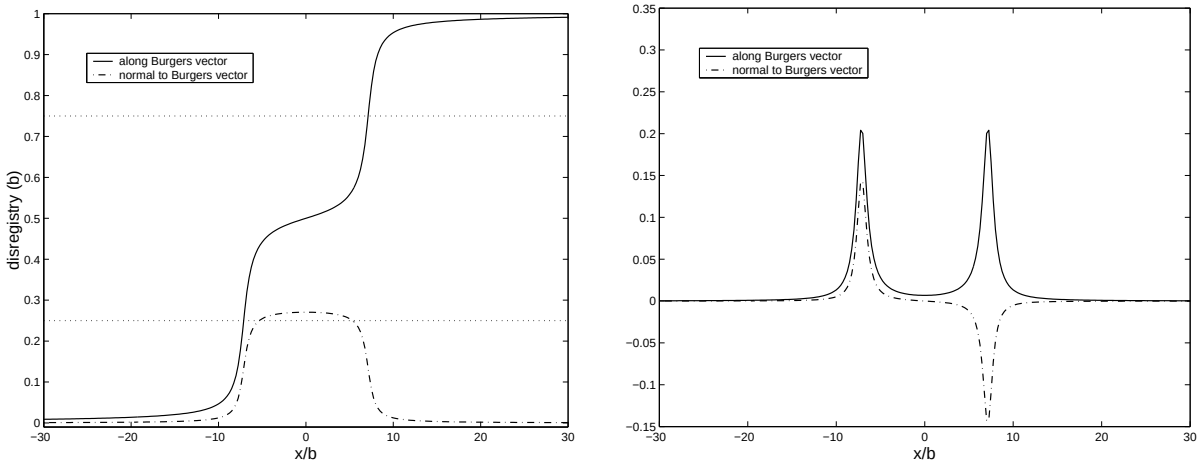

(a) Disregistry (b) Dislocation density

Fig. 4. The core structure of a straight edge dislocations in Cu. Solid line: the component parallel to the Burgers vector; Dash-dot line: the component perpendicular to the Burgers vector. The dotted lines in (a) show the values $\frac{1}{4}b$ and $\frac{3}{4}b$.

dislocations in Al are shown in Table 1, in which we have followed Lu *et al*. [11] to measure the dislocation core width by the distance over which the disregistry in the direction of the Burgers vector changes from $\frac{1}{4}b$ to $\frac{3}{4}b$. To obtain such a solution using the full two dimensional model, it took about 10 minutes in a simulation cell with 512×512 grid points or about an hour in a simulation cell with 1024×1024 grid points, on a personal computer with 3.2 GHz CPU and 4 GB memory.

The heavy overlap of the two Shockley partials in perfect dislocations in Al observed in our simulations is in agreement with the large value of the stacking fault energy in Al [1], and the simulation results in [11] using the semidiscrete Peierls-Nabarro model [9] and the generalized stacking fault energy from *ab initio* calculations. Our results of the core width shown in Table 1 agree very well with those obtained in [11], which are 0.70nm, 0.60nm, 0.50nm, and 0.42nm for the edge, 60^o, 30^o, and screw dislocations, respectively. This agreement validates the approximations of isotropic elasticity and the constrained path (i.e., neglecting the disregistry normal to the Burgers vector) for straight dislocations in Al used in [11].

The core structure of a straight edge dislocation in Cu obtained using our model is shown in Fig. 4. It can be seen that the edge dislocation in Cu dissociates clearly into two Shockley partials, which is quite different from the perfect dislocations in Al, see Fig. 3. The results of the separation of the two Shockley partials of different kinds of straight dislocations in Cu are shown in Table 1, where the partial separation is also identified by the distance over which the disregistry in the direction of the Burgers vector changes from $\frac{1}{4}b$ to $\frac{3}{4}b$.

The clear dissociation of perfect dislocations in Cu into two Shockley partials observed in our simulations is due to the low stacking fault energy in Cu [1], and has been observed in experiments [41]. The values of the partial separation obtained using our method shown in Table 1 agree with the experimental results [41] of 3.8 ± 0.6 nm for the edge dislocation and 1.8 ± 0.6 nm for the screw dislocation.

5 Dislocation loops

In this section, we report the simulation results of the core structure of dislocation loops in Al and Cu. The x axis is in the $[\bar{1}10]$ direction, which is in the direction of the Burgers vector, and the y axis is in the $[\bar{1}\bar{1}2]$ direction. The loop center is located at the origin.

For a dislocation loop, a constant shear stress is needed to prevent the loop from shrinking. The resulting unstable equilibrium configuration gives local maximum of the total energy. In order to obtain this unstable configuration of the dislocation loop, a Lagrange multiplier is used to keep the area enclosed by a dislocation loop constant during the energy minimization. The control area is proportional to the integral of the disregistry in the direction of the Burgers vector ϕ. The resulting Lagrange multiplier is thus the applied stress. For a very small perfect loop (or partial loop) whose maximum value of ϕ is less than b (or the length of the Burgers vector of the partial loop), it is more effective to control the value of ϕ at the center of the loop by varying the applied stress. Convergence tests show that the effect of the periodic boundary conditions is negligible for the core structure of dislocation loops with average radius up to about 1/4 of the size of the simulation cell with the parameters given in Section 3. The results reported here are based on the simulations of these loops.

5.1 Dislocation loops in Al

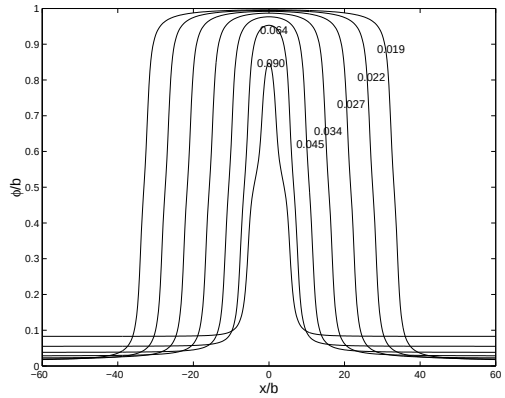

(a) Disregistry ϕ along the x axis.

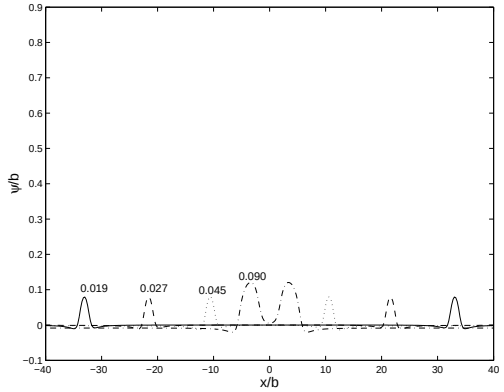

(b) Disregistry ψ along the x axis.

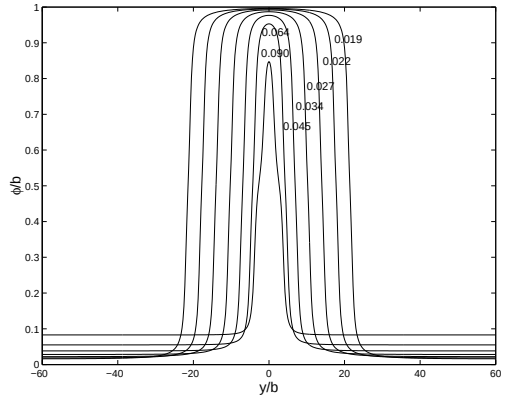

(c) Disregistry ϕ along the y axis.

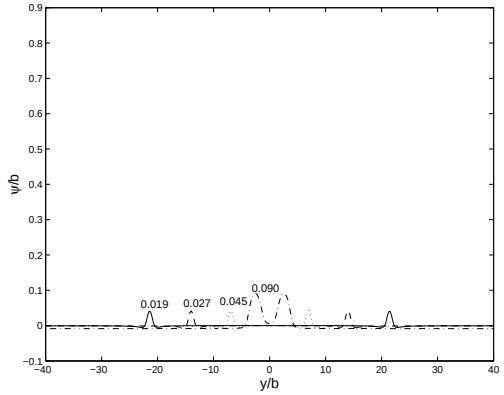

(d) Disregistry ψ along the y axis.

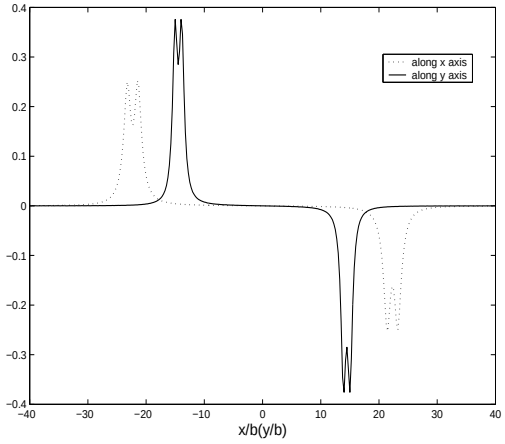

(e) Dislocation density of a perfect loop with applied stress $0.026\mu_{111}$.

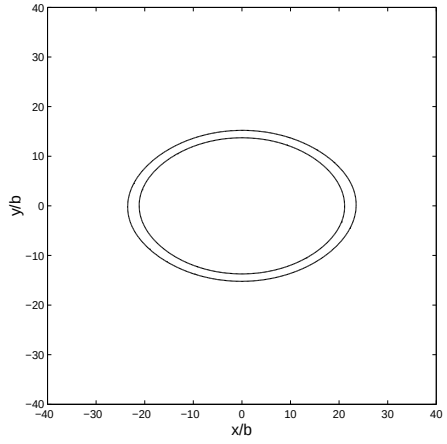

(f) Core region of a perfect loop with applied stress $0.026\mu_{111}$.

Fig. 5. Core structure of perfect dislocation loops in Al with different values of applied stress. The number associated with each curve in (a)–(d) is the value of the applied stress in the unit μ_{111}.

The core profiles of perfect dislocation loops in Al with different values of applied stress are shown in Fig. 5. Figure 5(a) and (c) show the disregistry ϕ, which is in the direction of the Burgers vector and determines the dislocation loops. Figure 5(b) and (d) show the disregistry ψ, which is in the direction perpendicular to the Burgers vector. The values of ψ are very small compared with the values of ϕ for these perfect loops, which validates the constrained path approximation (i.e., neglecting the disregistry normal to the Burgers vector) used in [21,27] for Al. As an example, the dislocation density and the core region of a perfect loop with applied stress $0.026\mu_{111}$ are shown in Fig. 5(e) and (f), where μ_{111} is the shear modulus in the $\{111\}$ plane of Al. The core region is identified by the region between the contour lines of $\phi = \frac{b}{4}$ and $\phi = \frac{3}{4}b$ as the straight dislocations in Al. We can see that in these perfect dislocation loops, the two Shockley partials are not clearly separated, only some tendency of splitting is shown, as in the straight perfect dislocations in Al. These perfect loops are elongated in the direction of the Burgers vector (the x direction), which agrees with the classical dislocation theory that the edge dislocations have larger line energy than the screw dislocations [1].

Partial dislocation loops in Al with Burgers vector $\frac{a}{6}[\bar{2}11]$ are also found in our simulations, as shown in Fig. 6. These partial loops are elongated along the 60^o direction with respect to the x axis, which is the direction of their Burgers vector $\frac{a}{6}[\bar{2}11]$.

The perfect and partial dislocation loops shown in Figs. 5 and 6 exist up to some critical applied stress levels. Under a large applied stress close to the critical levels, the loop is very small and its maximum value of ϕ is clearly less than b or the length of the Burgers vector of the partial loop, e.g., see the perfect loop with applied stress $0.090\mu_{111}$ shown in Fig. 5 or the partial loop with applied stress $0.127\mu_{111}$ shown in Fig. 6. In this case, the dislocation loops are not fully developed and the concept of the core region is not appropriate. The perfect or partial loops larger than those shown in these figures exist under lower values of the applied stress, and the profiles are similar to those of the largest loops shown in these figures. These are the same for the dislocation loops in Cu to be shown in the next subsection. More on the energetics of these two families of loops and the critical levels of the applied stress can be found in the next section.

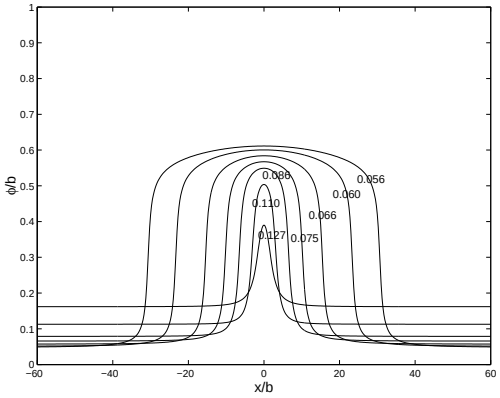

(a) Disregistry ϕ along the x axis.

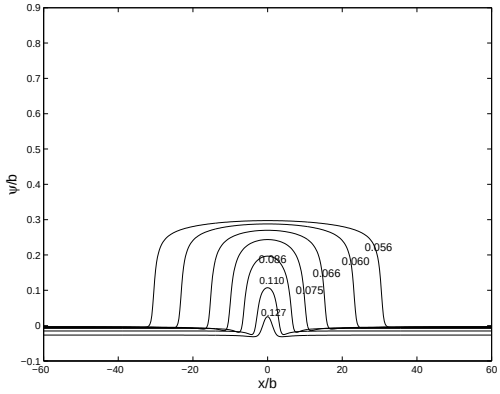

(b) Disregistry ψ along the x axis.

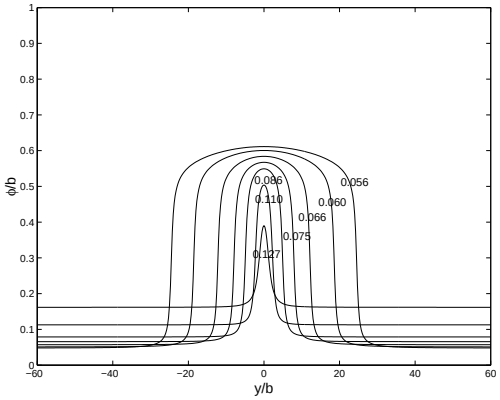

(c) Disregistry ϕ along the y axis.

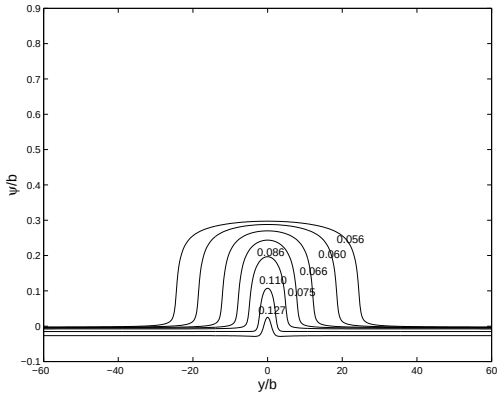

(d) Disregistry ψ along the y axis.

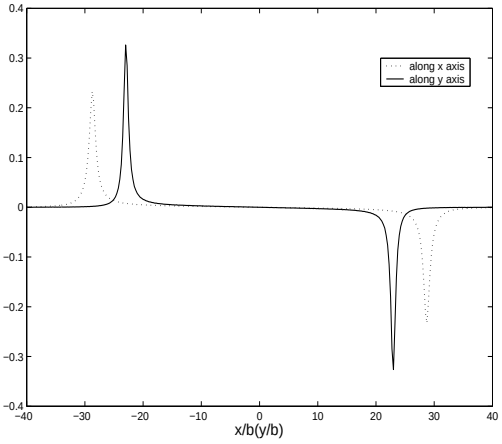

(e) Dislocation density of a partial loop with applied stress $0.057\mu_{111}$.

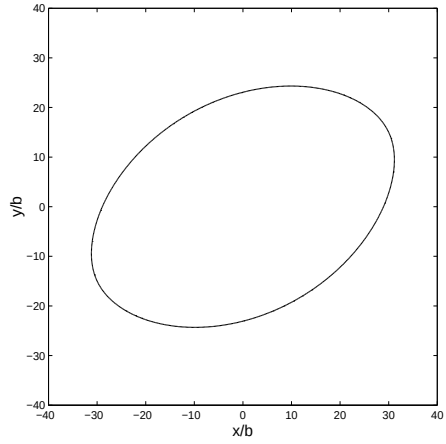

(f) Partial loop with applied stress $0.057\mu_{111}$.

Fig. 6. Core structure of partial dislocation loops in Al with different values of applied stress. The number associated with each curve in (a)–(d) is the value of the applied stress in the unit μ_{111}. The partial loop in (f) is identified by the contour line of $\phi = \frac{b}{4}$.

5.2 Dislocation loops in Cu

The core profiles of perfect dislocation loops in Cu with different values of applied stress are shown in Fig. 7. Figure 7(a)–(d) show the disregistry components ϕ and ψ along

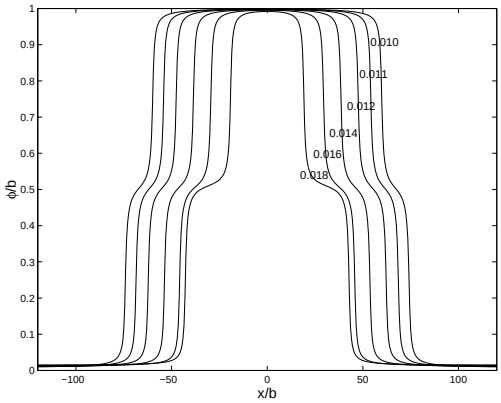

(a) Disregistry ϕ along the x axis.

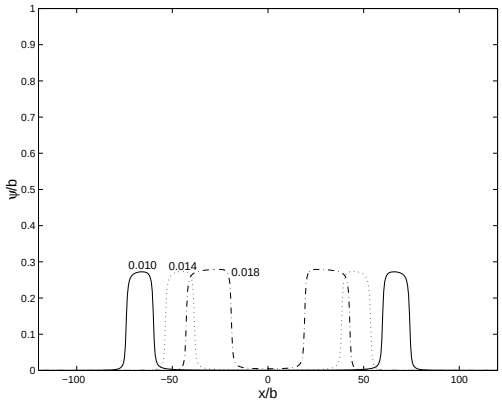

(b) Disregistry ψ along the x axis.

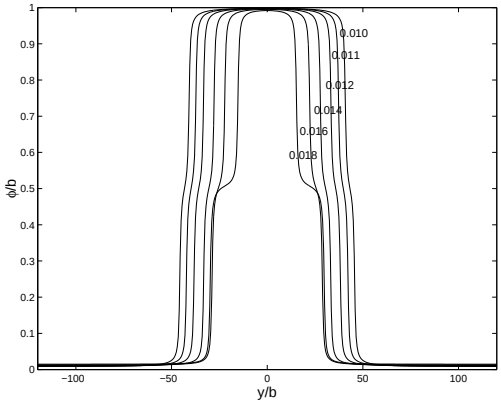

(c) Disregistry ϕ along the y axis.

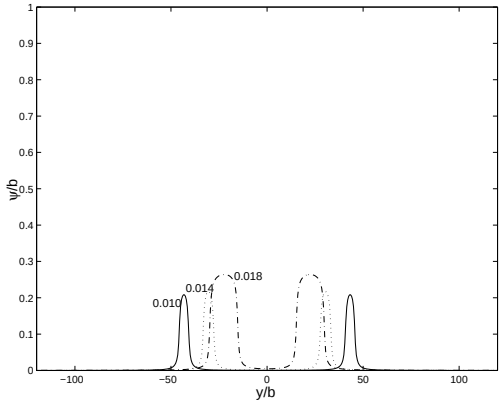

(d) Disregistry ψ along the y axis.

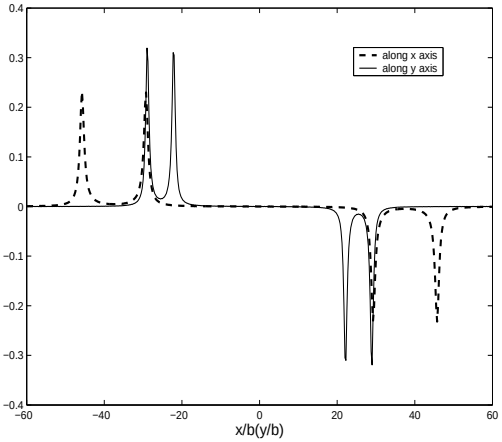

(e) Dislocation density of a perfect loop with applies stress $0.016\mu_{111}$.

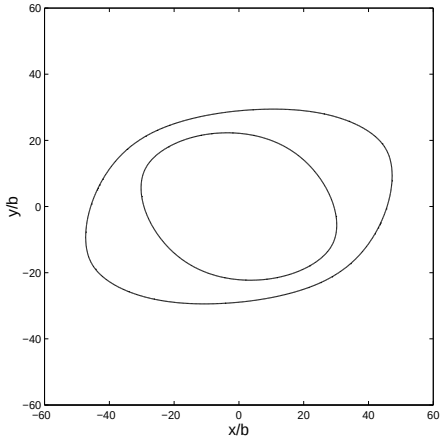

(f) Partial dissociation of a perfect loop with applies stress $0.016\mu_{111}$.

Fig. 7. Core structure of perfect dislocation loops in Cu with different values of applied stress. The number associated with each curve in (a)–(d) is the value of the applied stress in the unit μ_{111}.

the x and y axes. As an example, the dislocation density and the partial dissociation of a perfect loop with applied stress $0.016\mu_{111}$ are shown in Fig. 7(e) and (f), where μ_{111} is the shear modulus in the $\{111\}$ plane of Cu. The two partial loops shown in Fig. 7(f) are identified by the contour lines of $\phi = \frac{b}{4}$ and $\phi = \frac{3}{4}b$, respectively. These results show that unlike in Al, the two Shockley partials of a perfect dislocation loop in Cu are clearly separated, with Burgers vectors $\frac{a}{6}[\bar{2}11]$ ($(\phi, \psi) = (b/2, \sqrt{3}b/6)$) and $\frac{a}{6}[\bar{1}2\bar{1}]$ ($(\phi, \psi) = (b/2, -\sqrt{3}b/6)$) for the outer and inner partial loops, respectively. Between the two partial loops is the stacking fault region, where the disregistry (ϕ, ψ) is close to $(b/2, \sqrt{3}b/6)$, in contrast with the very small ψ for the perfect loops in Al shown in Fig. 5 (b) and (d). From these figures we can see that the partial dissociation along the y axis, where the dislocations are pure screw, is not as much as that along the x axis, where the dislocations are pure edge. This behavior is the same as that of the straight dislocations in Cu, see Table 1. These dissociated dislocation core structures in Cu cannot be obtained using the constrained path approximation, as was used for the dislocation core structures in Al in the literature [21,27].

In Fig. 7(f), the two partial loops of the perfect loop in Cu are elongated approximately in the directions of their own Burgers vectors, respectively. This behavior is quite different from that of the undissociated or slightly dissociated perfect loops in Al, in which the two partial loops together with the perfect loops are all elongated in the direction of the Burgers vector of the perfect loops, see Fig. 5(f). For a small perfect loop in Cu, the two partials are almost decoupled and elongated in the directions of their own Burgers vectors, due to the strong line tension effect of the two partials. As the size of the perfect loop increases, the line tension effect of the two partial loops becomes weak and the interaction between them becomes dominant, which makes them tend to elongated uniformly in the direction of the Burgers vector of the perfect loop. Compared with the perfect loops in Al, the tendency towards decoupling still exists for fairly large perfect loops in Cu (e.g. a perfect loop with radius about $100b$ in the x direction) due to the widely separated partials with relatively weak interaction between them. While for Al, this decoupling can only be seen in very small loops that are not fully developed (e.g. the perfect loop with applied stress $0.090\mu_{111}$ in Al).

The core profiles of partial dislocation loops in Cu with Burgers vector $\frac{a}{6}[\bar{2}11]$ obtained using our model are shown in Fig. 8. As in Al, these partial loops are elongated in the direction of their Burgers vector, and in some range of applied stress values, both the per-

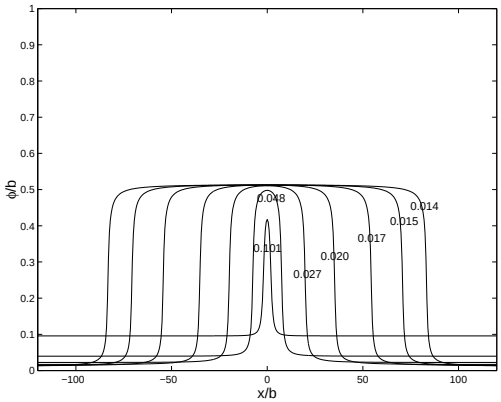

(a) Disregistry ϕ along the x axis.

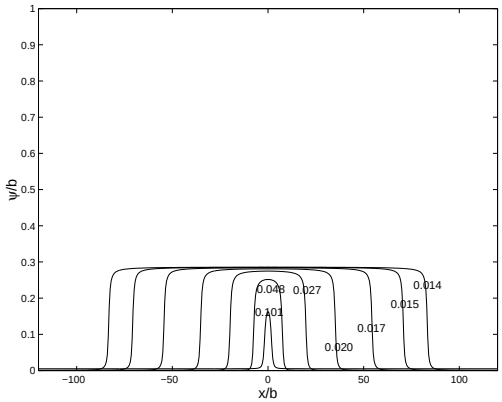

(b) Disregistry ψ along the x axis.

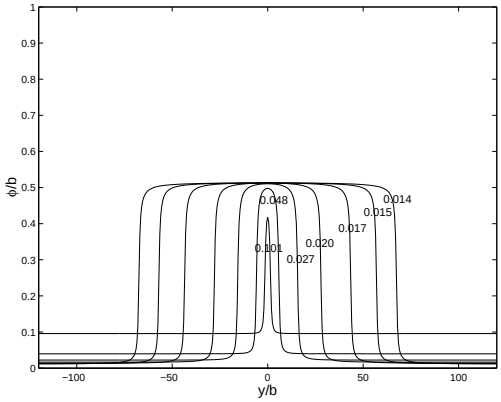

(c) Disregistry ϕ along the y axis.

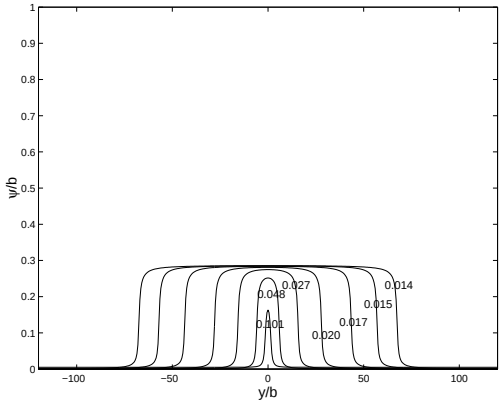

(d) Disregistry ψ along the y axis.

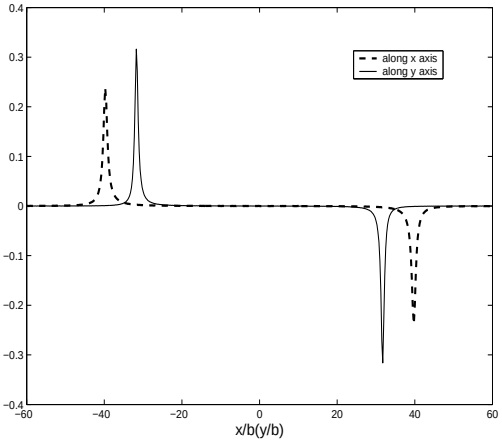

(e) Dislocation density of a partial loop with applies stress $0.019\mu_{111}$.

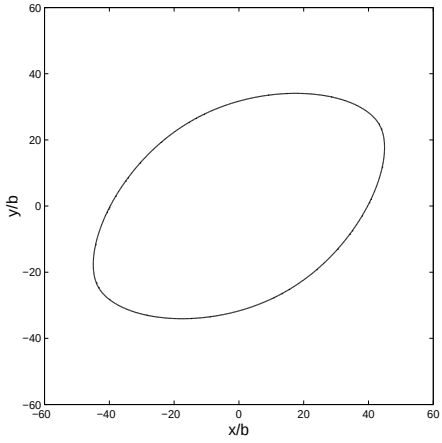

(f) Partial loop with applies stress $0.019\mu_{111}$.

Fig. 8. Core structure of partial dislocation loops in Cu with different values of applied stress. The number associated with each curve in (a)–(d) is the value of the applied stress in the unit μ_{111}. The partial loop in (f) is identified by the contour line of $\phi = \frac{b}{4}$.

fect and partial loops exist. The energetics of these two families of loops will be discussed in the next section.

6 Activation energies

It has been shown by continuum dislocation theory that homogeneous nucleation of dislocation loops in a perfect crystal by thermal activation is considered impossible under realistic values of applied shear stress due to the high activation energy [1]. This conclusion was confirmed by more accurate calculations of the activation energy using a variational method based on the Peierls-Nabarro framework [21]. However, in the calculations in [21], approximations of isotropic elasticity and sinusoidal interplanar potential with the constrained path (i.e., neglecting the disregistry normal to the Burgers vector ψ in the slip plane) were used. In this section, we calculate the activation energy of the dislocation loops in the {111} planes in Al and Cu using our model, incorporating elastic anisotropy and more realistic generalized stacking fault energy with the full disregistry in the slip plane.

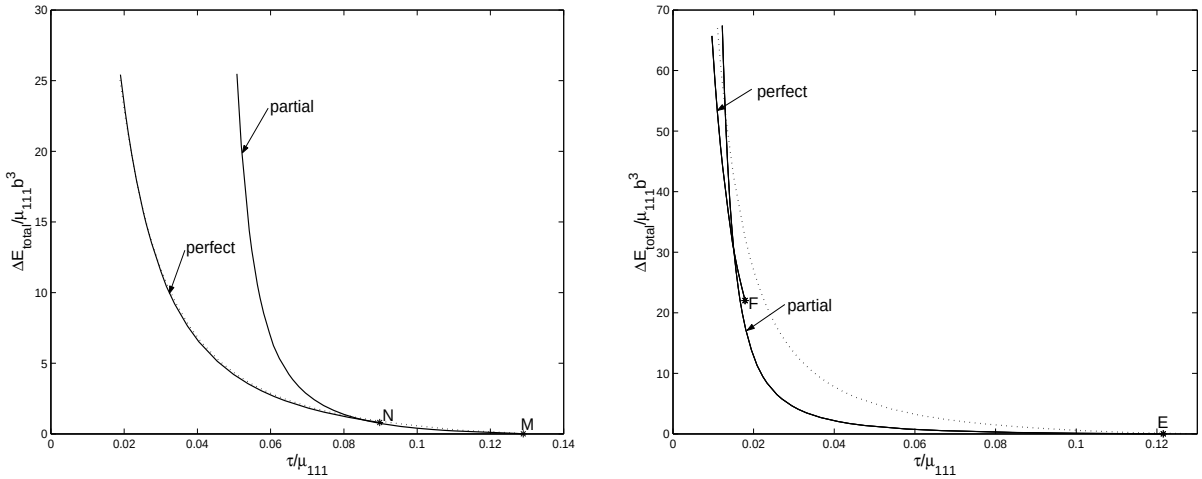

(a) Al (b) Cu

Fig. 9. Activation energies of dislocation loops in Al and Cu with different values of applied shear stress, and comparison with the constrained path approximation (dotted lines).

Following Xu and Argon [21], the activation energy is the difference between the total energy of the dislocation loop and that of the uniform stable shear deformation with the same applied stress level. The total energy is

$$E_{\text{total}} = E_{\text{elastic}} + E_{\text{misfit}} + E_{\text{applied}}, \tag{15}$$

where the elastic energy E_{elastic} and the misfit energy E_{misfit} are given by Eqs. (2) and (5) in Sec. 2, and the energy due to the applied stress E_{applied} is

$$E_{\text{applied}} = \int_{\mathbf{R^2}} [\sigma_{13}^{\text{app}} \phi(x,y) + \sigma_{23}^{\text{app}} \psi(x,y)] dxdy, \tag{16}$$

where σ_{13}^{app} and σ_{23}^{app} are the components of the applied stress. As in the previous section, in our simulations, the Burgers vector of the perfect dislocation loops is in the $+x$ direction, σ_{13}^{app} is constant, and $\sigma_{23}^{\text{app}} = 0$. It is known that there exists a critical value τ_c of the applied stress σ_{13}, above which no stable uniform deformation exists and slip occurs over the whole slip plane at once [1,4,21,25].

The activation energies for dislocation loops in Al and Cu obtained using our model are shown in Fig. 9. It is found that there are two branches of the activation energy curves when the applied stress is less than the critical applied stress τ_c, which is $0.13\mu_{111}$ for Al and $0.12\mu_{111}$for Cu (points M and E in Fig. 9). One branch starts from τ_c, along which partial loops are developed from loops with small disregistry as the applied stress decreases. The profiles of the partial dislocation loops and the loops with small disregistry in this branch are shown in Figs. 6 and 8 for Al and Cu, respectively. Perfect dislocation loops are developed along the other branch of the energy curve, starting from another critical applied stress value τ_p, which is less than τ_c and is $0.0898\mu_{111}$ for Al and $0.0179\mu_{111}$ for Cu (points N and F in Fig. 9). At the applied stress level τ_p, the activation energy for the perfect loop is larger than that for the partial loop. The profiles of the perfect dislocation loops in this branch are shown in Figs. 5 and 7 for Al and Cu, respectively.

When the applied stress level is less than τ_p, both the branches of the perfect loops and the partial loops exist. The two branches of energy curves intersect at an applied stress level τ_0, which is $0.0853\mu_{111}$ for Al and $0.0144\mu_{111}$ for Cu. When the applied stress is less than τ_0, the perfect loops are energetically favorable; when the applied stress is between τ_0 and τ_p, the partial loops are energetically favorable. For Al, the two branches of energy curves intersect almost at the starting point of the branch of perfect loops, which means that in Al, the perfect loops, if they exist, are almost always energetically favorable than isolated partial loops. Note that since the stacking fault region inside a partial loop is a local minimum energy state, there is an energy barrier for the nucleation of the second partial loop inside the original partial loop to form a perfect one, even though in most cases the perfect loop has lower energy than the initial partial loop at the same applied

Table 2
The activation energy of some dislocation loops in Al and Cu.

	Al perfect loop	Al partial loop	Cu perfect loop	Cu partial loop
Applied stress (μ_{111})	0.034	0.060	0.018	0.027
Activation energy (eV)	34	25	93	24

stress level.

In our simulations, we have considered the full disregistry vector (ϕ, ψ) in the slip plane, where ϕ and ψ are the components parallel and perpendicular to the given Burgers vector, respectively. We have also examined the previously used constrained path approximation [21,27], and the resulting energy curves are shown by the dotted lines in Fig. 9, along which perfect dislocation loops without dissociation are developed. For Al, the dotted line almost agrees with the energetically favorable parts of the two branches of energy curves with full disregistry, which verifies the constrained path approximation used previously for Al [21,27]. While for Cu, the constrained path approximation has a large error and does not give the energetically favorable partial loops. Thus it is very important to incorporate the full disregistry for the quantitative study of dislocation nucleation in Cu.

The values of activation energy of some dislocation loops in Al and Cu are shown in Table 2. These loops are among the smallest fully developed perfect or partial loops, see Figs. 5–8. These high values of activation energy confirm the conclusion that thermal activation plays negligible role in homogeneous nucleation of dislocation loops in a perfect crystal [1,21].

Our method and results provide a basis for accurate analysis of the nucleation of dislocation loops combined with other effects such as the presence of cracks [25,42,43] or surfaces [44,45].

7 Summary and discussion

We have proposed a generalized Peierls-Nabarro model for curved dislocations, in which the anisotropic elastic energy is obtained efficiently by solving the elasticity system associated with the disregistry across the slip plane using the FFT method, and the generalized stacking fault energy incorporating the full disregistry vector in the slip plane is used for

the interplanar potential. We have used this method to study the core structures and activation energies of dislocation loops in FCC Al and Cu.

Further generalization of this model may include the incorporation of the opening [9], the Peierls energy and the Peierls stress [9,17], the nonlocal effect near the slip plane [18], and multiple slip planes [20], as have been done for straight dislocations. This model can also be generalized to the study of structure and activation energy of curved dislocations near crack tips [25,42,43] or crystal surfaces [44,45].

Acknowledgements

The work of Y. Xiang is partially supported by the Hong Kong Research Grants Council CERG 603706. The work of P.B. Ming is partially supported by the National Natural Science Foundation of China under the grant 10571172 and also supported by the National Basic Research Program under the grant 2005CB321704. The work of W. E is supported by ONR grant N00014-01-1-0674 and NSF grant DMS04-07866.

References

[1] Hirth JP, Lothe J. Theory of Dislocations, 2nd ed. New York: John Wiley, 1982.

[2] Peierls R. Proc Phys Soc 1940;52:34.

[3] Nabarro FRN. Proc Phys Soc 1947;59:256.

[4] Frenkel J. Z Phys 1926;37:572.

[5] Vitek V. Phil Mag 1968;18:773.

[6] Kaxiras E, Duesbery MS. Phys Rev Lett 1993;70:3752.

[7] Joos B, Ren Q, Duesbery MS. Phys Rev B 1994;50:5890.

[8] Juan YM, Kaxiras E. Phil Mag A 1996;74:1367.

[9] Bulatov VV, Kaxiras E. Phys Rev Lett 1997;78:4221.

[10] Hartford J, von Sydow B, Wahnstrom G, Lundqvist BI. Phys Rev B 1998;58:2487.

[11] Lu G, Kioussis N, Bulatov VV, Kaxiras E. Phys Rev B 2000;62:3099.

[12] Schoeck G. Phil Mag A 1994;69:1085.

[13] Schoeck G, Krystian M. Phil Mag 2005;85:949.

[14] Eshelby JD. Phil Mag 1949;40:903.

[15] Seeger A, Schoeck G. Acta Metall 1953;1:519.

[16] Movchan AB, Bullough R, Willis JR. Eur J Appl Math 1998;9:373.

[17] Schoeck G. Phil Mag A 1999;79:2629.

[18] Miller R, Phillips R, Beltz G, Ortiz M. J Mech Phys Solids 1998;46:1845.

[19] Ngan AHW. J Mech Phys Solids 1997;45:903.

[20] Lu G, Bulatov VV, Kioussis N, Phil Mag 2003;83:3539.

[21] Xu G, Argon AS. Phil Mag Lett 2000;80:605.

[22] Xu G, Ortiz M. Int J Numer Meth Eng 1993;36:3675.

[23] Xu G. J Appl Mech 2000;67:403.

[24] Lothe J. Phil Mag A 1982;46:177.

[25] Rice JR. J Mech Phys Solids 1992;40:239.

[26] Movchan AB, Bullough R, Willis JR. Phil Mag 2003;83:569.

[27] Banerjee S, Ghoniem N, Lu G, Kioussis N. Phil Mag 2007;87:4131.

[28] Wang YU, Jin YM, Cuitino AM, Khachaturyan AG. Acta Mater 2001;49:1847.

[29] Koslowski M, Cuitino AM, Ortiz M. J Mech Phys Solids 2002;50:2597.

[30] Shen C, Wang Y. Acta Mater 2004;52:683.

[31] Nye JF. Acta Metall 1953;1:153.

[32] Kröner E. Z Phys 1958;151:504.

[33] Mura T. Micromechanics of Defects in Solids. Dordrecht: Martinus Nijhoff Publishers, 1987.

[34] Ming PB, Xiang Y, Yang Z, E W. to appear.

[35] Rose JH, Ferrante J, Smith JR. Phys Rev Lett 1981;47:675.

[36] Needleman A. J Mech Phys Solids 1990;38:289.

[37] Beltz GE, Rice JR. In: Lowe TC, Rollett AD, Follansbee PS, Daehn GS, editors. Modeling the Deformation of Crystalline Solids. Warrendale, Pennsylvania: Metallurgical Society of AIME, 1991. p.457.

[38] Bozzolo G, Ferrante J, Smith JR. Scripta Metall 1991;25:1927.

[39] Fung YC. Foundations of Solid Mechanics. Englewood Cliffs: Prentice-Hall, 1965.

[40] Zimmerman JA, Gao H, Abraham FF. Modelling Simul Mater Sci Eng 2000;8:103.

[41] Stobbs WM, Sworn CH. Phil Mag 1971;24:1365.

[42] Schoeck G. Phil Mag A 1991;63:111.

[43] Xu G, Argon AS, Ortiz M. Phil Mag A 1995;72:415.

[44] Gao H, Nix WD. Annu Rev Mater Sci 1999;29:173.

[45] Xu G, Zhang C. J Mech Phys Solids 2001;51:1371.